

Article

# Micromechanical Modeling for Predicting Residual Stress–Strain State around Nodules in Ductile Cast Irons

Andrew Ruggiero \*  and Ehsan Khademi 

Department of Civil and Mechanical Engineering, University of Cassino and Southern Lazio, Via G. Di Biasio, 43, 03043 Cassino, Italy; ehsan.khademi@unicas.it

\* Correspondence: a.ruggiero@unicas.it

**Abstract:** In this paper, a micromechanical model was developed to predict the residual stress–strain state that is generated around nodules of a ferritic ductile cast iron during solidification. A finite element analysis was performed on a reference volume element of the material to analyze the local strain development, having modeled both matrix and nodule as deformable bodies in contact. The behavior of the nodule was assumed linear–elastic because of the low stresses to which it is subjected during cooling. On the other hand, elasto-plastic viscous behavior was considered for the matrix, considering both the primary and secondary creep regimes. To make up for the lack of information on the physical–thermomechanical properties of the constituents, the available literature data were integrated with the results obtained from the CALPHAD methodology applied to both cast iron and the steel that constitutes its matrix. The micromechanical model was validated by comparing the resulting residual strains with experimental data available in the literature for a ferritic ductile cast iron. Then, it was used for analyzing the correlation between the solidification history and the mechanical response of cast iron in terms of the uniaxial stress–strain curve.

**Keywords:** ductile cast iron; micromechanics; constitutive modeling; creep; FEM



**Citation:** Ruggiero, A.; Khademi, E. Micromechanical Modeling for Predicting Residual Stress–Strain State around Nodules in Ductile Cast Irons. *Metals* **2023**, *13*, 1874. <https://doi.org/10.3390/met13111874>

Academic Editors: Guillaume Geandier, Alberto Campagnolo and Benoît Malard

Received: 9 October 2023

Revised: 30 October 2023

Accepted: 8 November 2023

Published: 10 November 2023



**Copyright:** © 2023 by the authors. Licensee MDPI, Basel, Switzerland. This article is an open access article distributed under the terms and conditions of the Creative Commons Attribution (CC BY) license (<https://creativecommons.org/licenses/by/4.0/>).

## 1. Introduction

Ductile Cast Irons (DCIs), because of their material characteristics, are increasingly considered an alternative to cast, forged, and welded steels for structural applications [1]. Their mechanical properties are strongly influenced by morphology and chemical composition as well as heat treatment that can be tuned to promote the desired microstructures [2–6]. Furthermore, improvements on material behavior can be achieved by imposing plastic deformation through hot or cold metal-forming processes [7,8].

These can range from one characterized by high ductility and impact toughness, as in EN-GJS-350 grade, to pearlitic structures with high strength and hardness, as in EN-GJS-900 grade [9].

Recently, new classes of high-performing DCIs are continually being developed and made commercially available. Some examples include the Austempered Ductile Irons (ADIs), with their strength-to-weight ratio exceeding that of aluminum [10], or the new grades of Si-alloyed DCIs, with increased strength and improved machinability, introduced in the European Standard EN 1563:2012 [11].

In an arena where optimizing the performance of DCIs is under continuous development, the availability of tools to predict their mechanical behavior is helpful to both foundry engineering and design. To this end, a micromechanical approach to analyzing the behavior of DCIs, which takes advantage of the composite nature of the material, has become established over the years [12–16]. In such an approach, the behavior of cast iron is obtained from that of its constituent materials. It is, therefore, particularly suited to assessing the effect of individual microstructural aspects on the overall response.

A Representative Volume Element (RVE) has to be defined at the microscale (i.e., in this case, the scale at which the dispersed nodules can be distinguished from the matrix)

and capable of reproducing the properties of the material at the macroscale (the scale of the continuum where the material can be seen as homogeneous). All microstructural aspects that influence global behavior must be appropriately modeled in this definition. These certainly include the volume fraction, components' constitutive response, and nodule–matrix interface behavior.

Regarding latter, since there is no chemical bond between the two components, the most widespread doctrine considers an interaction of pure mechanical nature between them. Bonora and Ruggiero [14] hypothesized that the mechanical interface forces are constituted by the residual stresses generated during the solidification of the DCI due to the mismatch between the thermal expansion coefficients of nodules and matrix. In the same work, for a ferritic cast iron, the residual stresses were calculated by simulating the cooling process from the temperature of 1000 °C, at which the matrix is considered stress-free, to room temperature.

Zhang et al. [17,18], using Differential Aperture X-ray Microscopy (DAXM), measured both local plastic and elastic residual strains in both metal and sand mold DCIs. The results, confirming the presence of residual stresses, suggest that they must be addressed in the analysis of the mechanical behavior of DCI, especially in facing applications involving fatigue, where their role is of primary importance. In this regard, Krasowsky et al. [19], using neutron diffraction monitoring of DCI under cyclic loading, demonstrated that as stress increased, the graphite inclusions promoted the nucleation of microcracks. Still, the residual compressive stresses surrounding them locally retarded fatigue crack growth.

Numerous studies have addressed the quantification of local residual stresses in DCI and the analysis of their effect on global behavior by pursuing increasing levels of refinement in finite element modeling of the RVE. Iannitti et al. [20] modeled an RVE considering a random dispersion of nodules that reflected the actual distribution measured in an ADI JS/1050-6. Andriollo et al. [21], using X-ray data, modeled the complete microstructure between two sections of a miniaturized DCI specimen and directly applied as boundary conditions the displacement field reconstructed by digital volume correlation.

The constitutive response of constituents should be appropriately described over the whole temperature range spanned in the simulation of the cast iron solidification process. Plastic strain development, confirmed by measurements in [17], affects the resulting residual stress state by relaxation. To properly quantify the amount of inelastic strain, it is necessary to employ refined models that fully consider the various physical mechanisms that influence mechanical strength. However, a significant limitation to their applicability lies in the lack of data on the physical–mechanical properties of the constituents at different temperatures.

The first problem is the unavailability of constituent materials for experimentation. Some attempts have been made to obtain steel with the same microstructure as the matrix of the considered cast iron, e.g., the ferritic steel manufactured in [22]. However, if with some limitations, though it can be achieved for the matrix, to date, obtaining the graphite that makes up the nodules as a stand-alone material has yet to be possible. Secondly, even if the fitting material is available, performing a complete characterization, especially at high temperatures, can be highly complicated and, when possible, very expensive.

In this work, to overcome such limitations, the physical and mechanical properties of the materials of interest were estimated by integrating literature data with predictions from a computational code. Specifically, the commercial code JMatPro (Java-based MATerials PROperties) was adopted. This uses the CALPHAD methodology (CALculation of PHASE Diagram [23]) to model the thermodynamic properties of the expected phases in the multi-component alloy and, from these, determine the thermodynamics of the alloy. Then, based on proprietary databases, the code correlates the calculated thermodynamic properties to the physical–mechanical properties of the alloy [24].

This approach was applied to the DCI analyzed by Zhang et al. [17] to calculate the basic properties of the matrix and nodules that are otherwise difficult to obtain. The constitutive modeling of the matrix was further refined to consider viscous creep, an aspect that has so far been treated limitedly in the literature (e.g., Andriollo et al. [22] addressed

creep by adopting Peric’s model) and implemented in the implicit finite element code MSC.MARC via user subroutine. Then, a numerical model of the RVE was built and used to simulate solidification. Results were validated by comparison with experimental measurements regarding distributions of inelastic and residual elastic strains developed into the matrix near the nodules. Finally, the developed micromechanical model was used to evaluate the weight that the main parts of the modeling have on the mechanical response of cast iron in terms of the uniaxial stress–strain curve at room temperature.

The steps of this work in sequential order are illustrated by the flowchart in Figure 1 for a comprehensive view of the overall process.

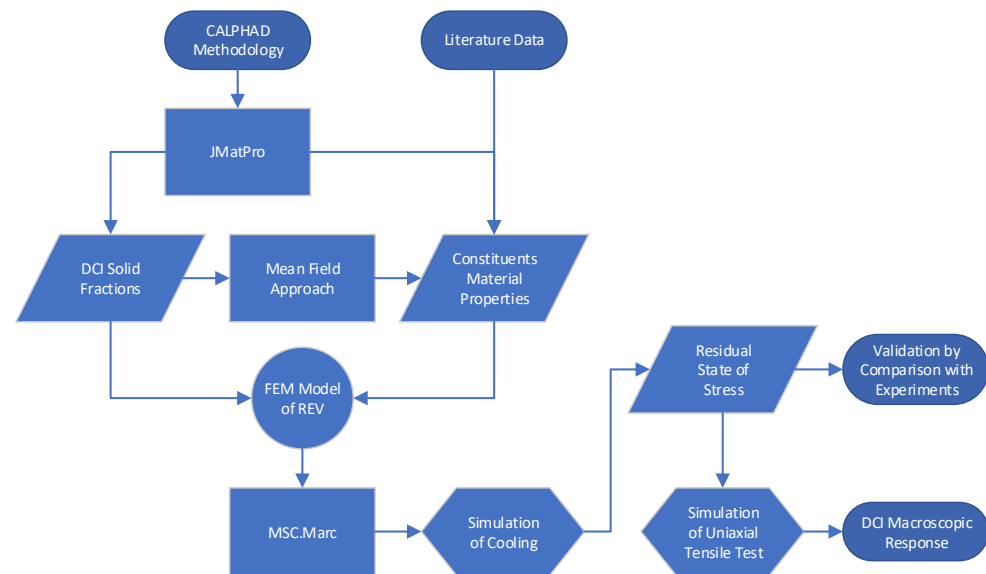


**Figure 1.** Flowchart of the separate steps of this work in sequential order.

## 2. Material and Constitutive Modeling

### 2.1. DCI

The material under investigation is the DCI analyzed in Zhang et al. [17], whose chemical composition is shown in Table 1. Full chill casting was used to process the ductile cast iron, utilizing a metal mold with approximate dimensions of 2.6 m × 2.6 m × 4.5 m and a wall thickness of 100–200 mm. The matrix is ferritic with a small volume fraction of perlite (about 5%). The average grain size is about 30 μm; the mean size diameter of graphite nodules is ~30 μm with a volume fraction of 11.5%.

The JMatPro code was used to obtain the general physical properties of the DCI. Chemical composition has been input in the code as in Table 1 with the exclusion of cobalt, cerium, and selenium, which the code does not consider. Although Co and Ce are graphitizing and spheroidizing elements, even for the low concentrations involved, all of them have negligible effects on the other properties of the alloy, both physical and thermodynamic. Since the graphite volume fraction is input to the calculation, not considering these elements does not affect the analysis results. To ensure the sphericity of nodules and avoid introducing an undesirable influence parameter such as spheroidicity, a high Mg content was used.

**Table 1.** Chemical composition of the DCI (in wt.%). Fe: balance.

C	Si	Mn	P	S	Cr	Ni	Co	Cu	Ti	V	Mg	Ce	Se
3.68	2.30	0.22	0.015	0.011	0.027	0.048	0.024	0.016	0.017	0.014	0.11	0.042	0.043

Then, the solidification was simulated by obtaining a pearlite–ferrite mixture and indicating a volume fraction of graphite of 11.5%, starting from a temperature of 1400 °C. Based on the CALPHAD methodology, with the given composition, the evolution of the solid fraction with cooling as in Figure 2 was calculated; the solid fractions at room temperature are reported in Table 2. No appreciable difference was found in considering or not considering the precipitation of second-phase particles.

Solidification ends at 1065 °C, where austenite and graphite are the only phases present. At 819 °C, austenite begins to transform into ferrite; at 790 °C, the growth of graphite nodules ends and the mass content of carbon in the form of graphite reaches the final value that will be valid until room temperature. At 765 °C, cementite begins to form; below 750 °C, austenite is no longer present and the weight fractions of the other phases stabilize at the value they will maintain until room temperature.

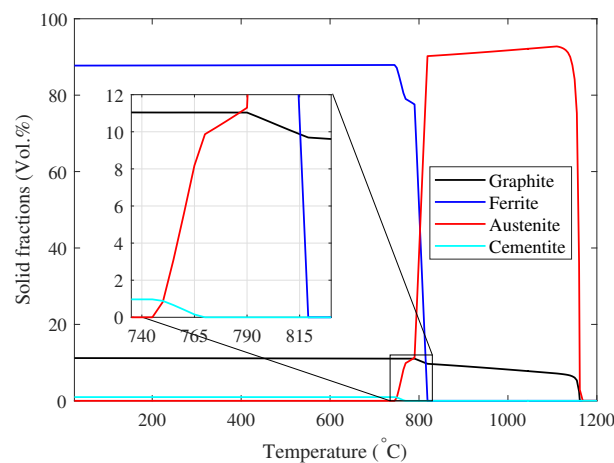


**Figure 2.** Variation of DCI solid fractions in Vol.% with temperature.

**Table 2.** DCI solid fractions at room temperature.

	Vol. %	Wt. %
Graphite	11.207	3.591
Ferrite	87.827	95.362
Cementite	0.966	1.048

Assuming that all cementite is present in the form of pearlite, the volume fraction of the latter can be derived from the values of Table 2 knowing that it is a two-phased, lamellar (or layered) structure composed of alternating layers of ferrite (87.5 wt%) and cementite (12.5 wt%). A solid fraction of cementite equal to 1.048 wt% requires a fraction of ferrite in the perlite equal to  $Fe_p = 7.334$  wt%. This amount is 0.077 of the total ferrite, and from this value, the volumetric fraction of ferrite in perlite (6.755%) can be calculated. Thus, the volumetric fraction of the perlite, obtained by adding this amount to the cementite, turns out to be 7.72%.

The volumetric fraction of graphite contained in nodules, as calculated by JMatPro, is slightly lower than measured (11.2% vs. 11.5%), while the contrary is true for pearlite (7.7% vs. 5%). Although slightly different, the solid fractions predicted by thermodynamic equilibrium are very close to those measured, so the calculated general physical properties can be considered reliable.

The estimates of elastic properties, however, seem to be less reliable. The Young's modulus calculated is 147.4 GPa. This is much less than that reported in the literature for a cast iron of the same grade, which is between 167 and 170 GPa; likewise, the calculated Poisson's ratio is 0.274, compared to 0.28 reported in the literature [15,25–31].

It is unclear whether these discrepancies, also found for other cast iron classes, are due to a deficiency in the database available to the code or whether they result from a different

interpretation in measuring the mechanical quantity. The nonlinearity of the stress–strain curve of cast iron, even below the yield strength, makes the figure highly dependent on the derivation method. In any case, given the apparent discrepancy, the elastic properties of cast iron were taken from the literature, neglecting the estimates obtained with JMatPro.

## 2.2. Matrix

### 2.2.1. Microstructure

In agreement with the solid fractions in Table 2, the carbon still available would be 0.09 wt% (0.093 wt% if related to the matrix alone). However, as noted in the previous paragraph, this amount overestimates the amount present. For more reliable estimation, matrix solidification was iteratively simulated with JMatPro by imposing different carbon contents to obtain the correct volume fraction of perlite. The solidification model used is based on the lever rule; the starting composition is the same as that considered in Table 1, with the fractions appropriately scaled with respect to proper carbon content. Magnesium, cerium, and selenium were excluded from the calculation since the code does not consider them.

Simulation results have shown that a carbon content of 0.058 wt% leads to general steel with a perlite volume fraction of 5.693%, which, for the cast iron with a graphite volume fraction of 11.5%, is equivalent to 5.06%. The estimated amount of carbon is not far from the 0.036 wt% used in [22] with the aim of obtaining a steel equivalent to the matrix of the analyzed DCI. The chemical composition obtained for the matrix is reported in Table 3.

**Table 3.** Chemical composition of matrix (in wt.%). Fe: balance.

C	Si	Mn	P	S	Cr	Ni	Co	Cu	Ti	V	Mg	Ce	Se
0.058	2.386	0.228	0.016	0.011	0.028	0.05	0.025	0.017	0.018	0.015	0.114	0.044	0.045

The variation of the solid fractions with temperature is shown in Figure 3. This material has the same chemical content as the matrix for temperature less than 790 °C, at which, as seen in the previous paragraph, the mass content of carbon in the form of graphite has reached its final value. For higher temperatures, the carbon in the cast iron matrix is higher, and the composition of Table 3 no longer represents that of the actual matrix.

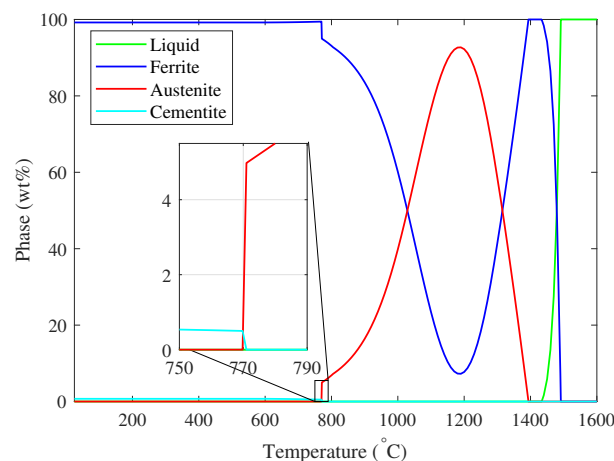


**Figure 3.** Variation of matrix phases in wt% with temperature.

At that temperature (790 °C), a residual amount of austenite (6.14 wt%) is still present, which completely decomposes below 770 °C. At 770 °C, cementite begins to form; at 769 °C, its solid fraction is already 0.5 wt% and increases slowly with cooling to a final value of about 0.71 wt%, reached at 600 °C. Solid fractions of the steel at room temperature are given in Table 4.

**Table 4.** Volume and weight fractions of matrix phases.

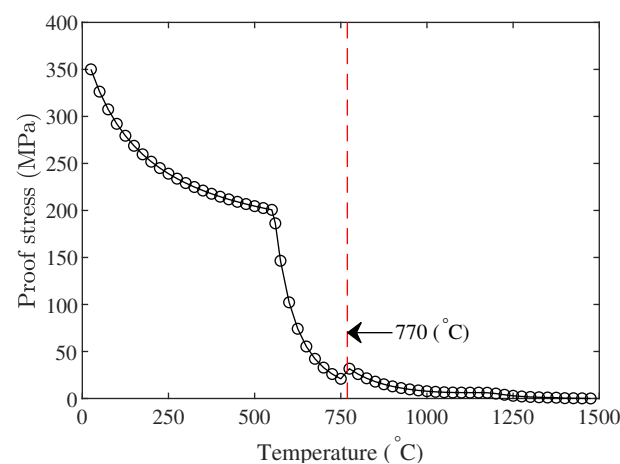
	wt. %	Vol. %
Ferrite	99.217	99.165
Cementite	0.71308	0.717
M <sub>6</sub> C	0.03939	0.06003
M <sub>N</sub> S	0.03093	0.05863

Since at 790 °C the nodules are fully formed and the chemical composition of the matrix is frozen, it is reasonable to consider that the simulation of cooling to determine the state of the residual stresses should begin at this temperature. However, although the matrix and the equivalent steel, under 790 °C, have the same chemical composition, they arrive at that temperature with different structures, and time associated with a thermal jump is required to reach solid fractions congruent with each other. Starting the simulation of solidification from a temperature very low would guarantee the congruity of the two structures; on the other hand, skipping the simulation of a significant part of cooling compromises a correct estimation of the residual stresses. A compromise solution was identified with the choice of starting the simulation from the lower eutectic of the steel (769 °C). At this temperature, the structure obtained is very close to the final structure and, at the same time, the jump between 790 °C and 769 °C is sufficiently tiny to assume, reasonably, the effect on residual stresses is negligible within the approximations of the analysis.

### 2.2.2. Mechanical Properties

Once the solid fractions are calculated, general physical and mechanical properties can be obtained. The values of Young modulus ( $E$ ), Poisson's ratio ( $\nu$ ), coefficient of thermal expansion (CTE), and density ( $\rho$ ) as functions of temperature are given in Appendix A.

Further, providing the final grain size, a matrix proof stress at room temperature of 350.72 MPa is calculated, from which its variation with temperature can be obtained; see Figure 4. In the plot, a sudden variation is observed at 770 °C, the temperature at which austenite (FCC structure) decomposes completely to favor ferrite (BCC structure).

**Figure 4.** Variation of matrix proof stress with temperature.

From the proof stress values, true stress–true strain curves for different strain rates and temperatures can be finally obtained. In Figure 5, calculated quasistatic curves for different temperatures are reported together with the experimental tensile curve, measured at room temperature in [32] for the matrix of the same grade of DCI. The comparison reveals excellent agreement, particularly for strains up to 0.2.

The description of the mechanical behavior of the matrix must be completed with the modeling of creep. Due to the short time of the cooling process, the transient strain

cannot be neglected compared to the steady state. This choice is in agreement with the classification proposed by Sherby and Bruke [33], in which Class II alloys, such as Fe-Si alloys, show a significant primary stage.

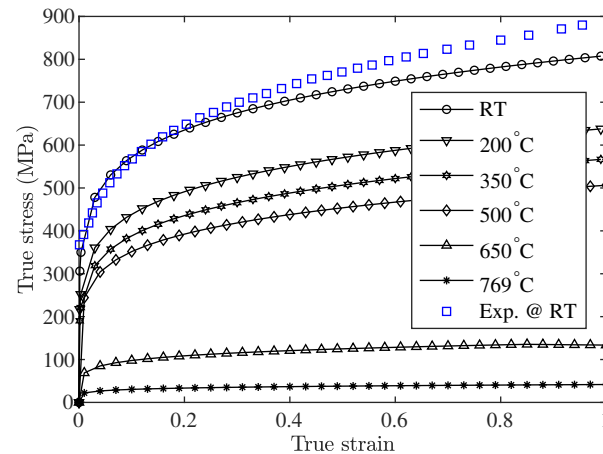


**Figure 5.** Calculated matrix flow curves at different temperatures (line and symbols) and experimental curve (symbols) at room temperature from [32].

For the material investigated, creep is not of application interest and therefore the amount of data available is minimal. This and the need to model the primary creep precluded using JMatPro for that modeling aspect. To account for the primary, the Esposito and Bonora model [34] was adopted, for which transient creep strain rate is a function of the steady-state creep rate:

$$\frac{\dot{\varepsilon}}{\dot{\varepsilon}_{ss}} = \exp \left[ \frac{\bar{\Omega}}{RT} \sigma \exp \left( -\frac{\varepsilon}{\varepsilon_0} \right) \right] \quad (1)$$

where the material coefficients  $\bar{\Omega}$  and  $\varepsilon_0$  denote, respectively, the scaled activation volume and the decay constant,  $\varepsilon$  is the creep strain, and  $\dot{\varepsilon}$  the creep strain rate. In this formulation, for specified reference stress and temperature, the lower bound of the creep rate in the transient region corresponds to the steady-state creep rate,  $\dot{\varepsilon}_{ss}$ . To describe the latter, in the present work, the following semi-empirical model for secondary creep rate has been taken as a starting point [35,36]:

$$\dot{\varepsilon}_{ss} = A \frac{DGb}{kT} \left( \frac{\sigma}{G} \right)^n \quad (2)$$

where  $A$  is dimensionless constant,  $D$  is self diffusivity,  $G$  is shear modulus,  $b$  is the Burgers vector,  $K$  is the Boltzmann constant,  $T$  is the absolute temperature,  $\sigma$  is the applied stress, and  $n$  is the stress exponent.

The model has been improved to account for effective stress,  $\sigma - \sigma_p$  as defined in [37,38]. Here,  $\sigma_p$ , called “back stress” or “friction stress”, represents the stress supported by substructural factors other than dislocations taking part in the creep deformation process, [38], such as subgrain or subcell sizes and particles dispersed in pure or alloy metals [39,40]. This concept implies that creep occurs only when effective stress is positive, whereas for applied stresses below  $\sigma_p$ , creep is negligible, [41], and can be ignored in modeling. Therefore, considering that secondary creep deformation in Equation (2) is driven by effective stress, the following rate-controlling relation can be proposed:

$$\dot{\varepsilon}_{ss} = A \frac{DGb}{kT} \left( \frac{\sigma - \sigma_p}{G} \right)^n \quad (3)$$

As stated before, the availability of creep data for the alloy under investigation is minimal. Among the few available works, Kaibyshev and Kazakulov [42] analyzed steel

with a composition very similar to that of the DCI matrix but with a different grain size, 6 mm versus 30  $\mu\text{m}$ .

Experimental analysis of Fe-Si with an amount of silicon comparable to that of the DCI matrix concluded that, even though some effects on the transient creep exist, grain size does not affect steady-state creep [43–45]. Accepting this limitation, the data in [42] were used to calibrate the model coefficients. In the procedure, the following aspects were considered. First, the simulated cooling occurs at temperatures lower than 800  $^{\circ}\text{C}$ ; therefore, deformation behavior at higher temperatures is out of the range of interest. Second, for temperatures lower than 550  $^{\circ}\text{C}$ , the stress required for creep to occur is exaggeratedly higher than those achieved in the cooling process. Therefore, coefficients were calibrated on data limited to the range mentioned above.

The first step is the calibration of the back stresses. From Equation (3), the relation between  $\dot{\epsilon}_{ss}^{(1/n)}$  and applied stress can be plotted; see Figure 6.

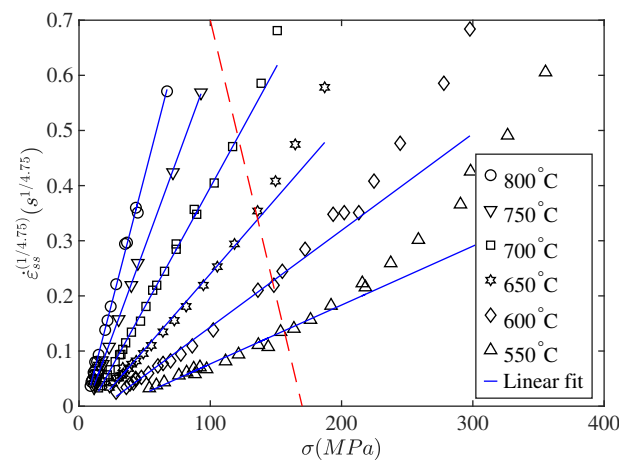


**Figure 6.** Relationship between  $\dot{\epsilon}_{ss}^{(1/n)}$  and  $\sigma$  for  $n = 4.75$ ; interpolations of experimental data from [42].

Here, the red dashed line indicates the stress up to which the relation is linear for each temperature, assuming a calibrated value of  $n = 4.75$ . Extrapolation to zero strain rate provides the relative back stresses values.

Their variation with the inverse of the temperature, reported in the semilogarithmic diagram in Figure 7, can be adequately described by the relation proposed by Mohamed et al. [46]:

$$\frac{\sigma_p}{G} = B \exp \frac{Q_p}{RT} \quad (4)$$

where  $B$  is a dimensionless constant,  $R$  the universal gas constant, and  $Q_p$  an energy term. The calibrated coefficients are shown in Table 5.

The self diffusivity parameter,  $D$ , according to [47], can be described by the Arrhenius equation:

$$D = D_0 \exp \frac{-Q}{RT} \quad (5)$$

where  $D_0$  is material constant and  $Q$  is the activation energy for inelastic deformation. For  $\alpha$ -iron, the following values can be adopted:  $D_0 = 2 \times 10^{-4}$  [38] and  $Q = 280$  [48].

In Figure 8, normalized steady-state strain rate  $\dot{\epsilon}_{ss}kT/(DGb)$  versus normalized effective stress  $(\sigma - \sigma_p)/G$  is plotted on a logarithmic scale, assuming  $b = 0.248$  nm for  $\alpha$ -Fe according to [49]. The linear fit of the data for  $(\sigma - \sigma_p)/G < 0.003$  allows the determination of the coefficient  $A$  and the verification of  $n$  for the region of interest in this paper; see Table 5. For completeness, in the same table, the calibrated coefficients for  $(\sigma - \sigma_p)/G > 0.003$  are also reported and identified with subscript 2. The existence of the two different techniques is also reported in [42,50].

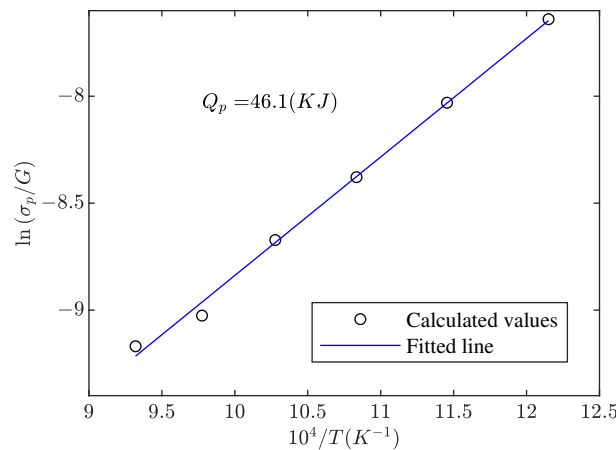


Figure 7. Variation of normalized back stress with temperature.

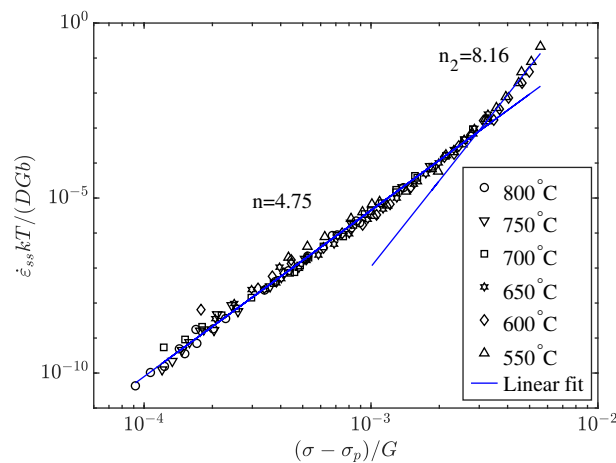


Figure 8. Normalized strain rate vs. normalized effective stress; interpolations of experimental data from [42].

Table 5. Steady-state creep constants.

$B$	$Q_p$ (KJ/mol)	$D_0$ (m <sup>2</sup> /s)	$Q$ (KJ/mol)	$n$	$A$	$n_2$	$A_2$
$5.69 \times 10^{-7}$	46.1	$2 \times 10^{-4}$	280	4.75	$7.9090 \times 10^8$	8.16	$3.3390 \times 10^{17}$

In Figure 9, the steady-state creep strain rates as a function of stress at different temperatures are shown. The comparison between experimental [42] and calculated data measures the effectiveness of the modeling adopted for stationary creep.

For calibration of the coefficients related to primary creep, it is convenient to rewrite Equation (1) in the form:

$$\ln \left[ \ln \left( \frac{\dot{\epsilon}}{\dot{\epsilon}_{ss}} \right) \right] = \ln \left( \frac{\bar{\Omega}}{RT} \sigma \right) - \left( \frac{\epsilon}{\epsilon_0} \right) \tag{6}$$

Kaibyshev and Kazakulov [42] also reported  $\dot{\epsilon}$  vs.  $\epsilon$  curves for the stress pairs of 78.9 and 99.3 MPa and 28.0 and 43.3 MPa, respectively, for the temperatures of 500 and 600 °C. Interpolations of these experimental data with Equation (6) give the values of the decay constant and scaled activation volume plotted in Figures 10 and 11, respectively. Both  $\bar{\Omega}$  and  $\epsilon_0$  are functions of applied stress, but are temperature-independent [34].

At least in the considered range, the decay coefficient variation with stress can be described with a linear relation:

$$\epsilon_0 = \bar{\epsilon}_0 + \frac{\sigma}{C_1} \tag{7}$$

While for scaled activation volume, an exponential decay was adopted:

$$\bar{\Omega} = \Omega_0 + C_2 \exp\left(-\frac{\sigma}{C_3}\right) \tag{8}$$

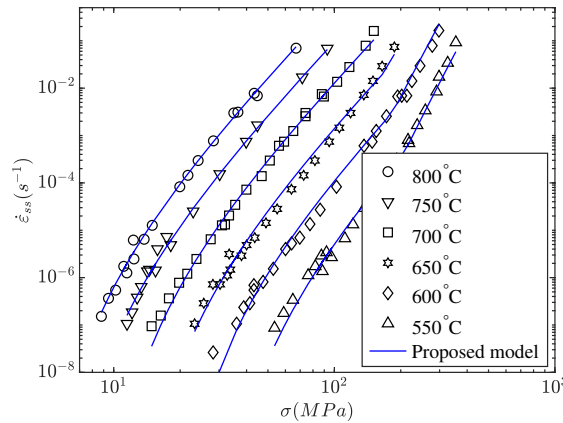


**Figure 9.** Variation in steady-state creep strain rates with stress at different temperatures: comparison between experimental data of [42] and proposed model.

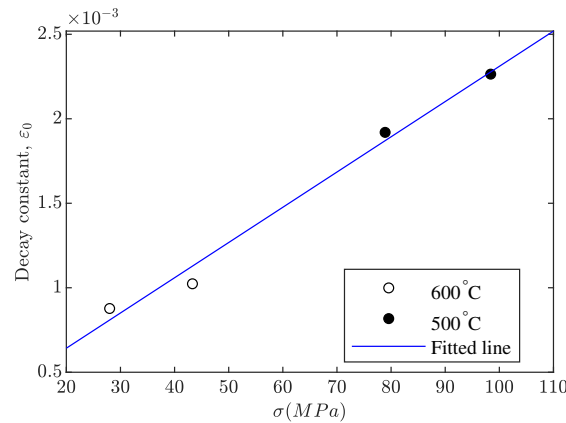


**Figure 10.** Variation of decay constant with applied stress; interpolation of experimental data at 500 °C and 600 °C from [42].

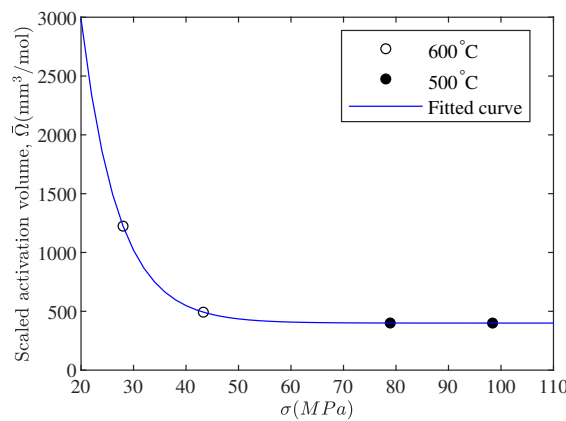


**Figure 11.** Variation of scaled activation volume with applied stress; interpolation of experimental data at 500 °C and 600 °C from [42].

Calibrated material coefficients for primary creep are given in Table 6.

**Table 6.** Transient creep coefficients.

$\bar{\epsilon}_0$ (mm/mm)	$C_1$ (MPa)	$\Omega_0$ m <sup>3</sup> /mole	$C_2$ m <sup>3</sup> /mole	$C_3$ (MPa)
$2.2515 \times 10^{-4}$	$4.7957 \times 10^4$	$4.0 \times 10^{-7}$	$4.5 \times 10^{-5}$	7

Comparison between experimental data, [42] and calculated creep strain rates, Figure 12, confirms the proposed model's correctness, which is effective in describing both transient and steady-state regimes.

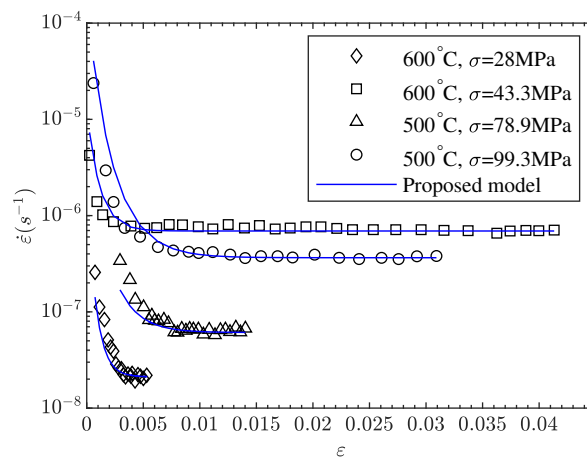


**Figure 12.** Creep strain rate versus creep strain: comparison between experimental data of [42] and proposed model.

### 2.3. Nodules

Since the bulk material of the nodule graphite is not available, information regarding its constitutive behavior is minimal. On this premise, the modeling was chosen to be as simple as possible. During solidification, the nodules are subject to extremely low stresses and marginal deformations. Therefore, they were modeled as homogeneous, isotropic, and elastic.

To determine the elastic constants, the mean-field approach was used by the commercial code Digimat-MF. For the matrix, elastic constants calculated in the previous section were fixed. For the nodule, a Young's modulus of 27 GPa was imposed in accordance with the estimate made by Hervas [51] based on microhardness measurements. Then, the Poisson ratio was varied iteratively until elastic constants for the DCI were consistent with what was presented in Section 2. Specifically, with a nodule Poisson's ratio of 0.22, values of  $E = 167.8$  GPa and  $\nu = 0.28$  are obtained for the DCI. The values determined can be considered constant with temperature, to a good approximation, over the range of interest. This result is consistent with the high melting temperature of graphite, 3700–5000 °C, depending on its microstructure and measurement method [52], when compared to that of steel matrix.

To verify the correctness of this assumption, the trend of the Young's modulus of the DCI with temperature, thus determined, was compared with experimental measurements reported by Delprete and Sesana [53], for a different grade of cast iron, scaling the data to room temperature values; see Figure 13. The agreement found confirms that the variation is dominated by the effect of temperature on the matrix response alone.

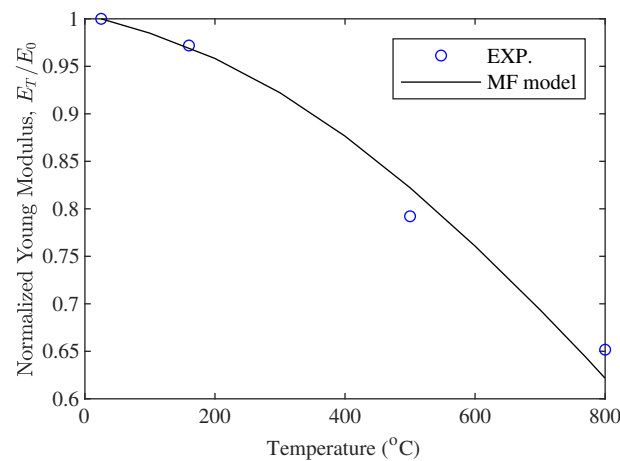


**Figure 13.** Variation of Young’s modulus with temperature for DCIs: comparison between experimental data after [53] and results of the mean-field homogenization.

Finally, the determination of CTE, which is fundamental to the type of analysis addressed in the paper, was addressed. In the literature, detailed measurements, over several temperature ranges, perpendicularly,  $\alpha_{\perp}$ , and parallel,  $\alpha_{\parallel}$ , to the axes of the hexagonal crystal of graphite are available. The CTE for graphite nodules was obtained by employing the data reported in Tsang et al. [54], using the relationship proposed by Riley [55] for polycrystalline graphite:

$$\bar{\alpha} = \frac{2}{3}\alpha_{\perp} + \frac{1}{3}\alpha_{\parallel} \quad (9)$$

Assuming a random orientation of the graphite structure, as in the case of polycrystals, agrees with the cone structure described by Monchoux et al. [56]. Calculated values for the temperature range of interest are shown in Figure 14.

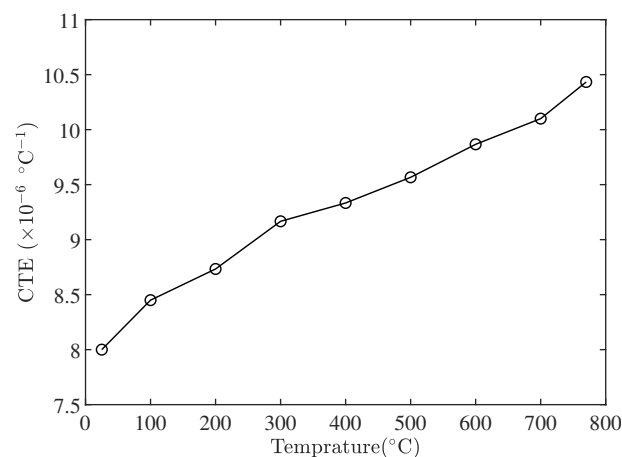


**Figure 14.** Graphite nodule CTE variation with temperature.

### 3. Numerical Modeling

Simulations were carried out with the implicit finite element code MSC.Marc.2021. For the RVE definition, the random distribution of nodules into the DCI matrix was reduced to a simple cubic (SC) cell structure (Figure 15a). The initial dimensions of the cell were chosen to have, at room temperature, a diameter of graphite nodules of 30  $\mu\text{m}$  and a volume fraction of 11.5%, corresponding to the average values for the DCI considered. This leads to a cell side  $L_0 = 49.723 \mu\text{m}$  at room temperature. Matrix and nodule were modeled as deformable bodies and discretized, respectively, with 13,312 and 2048 isoparametric hexahedral elements with 8 nodes and 8 Gauss points, Figure 15b.

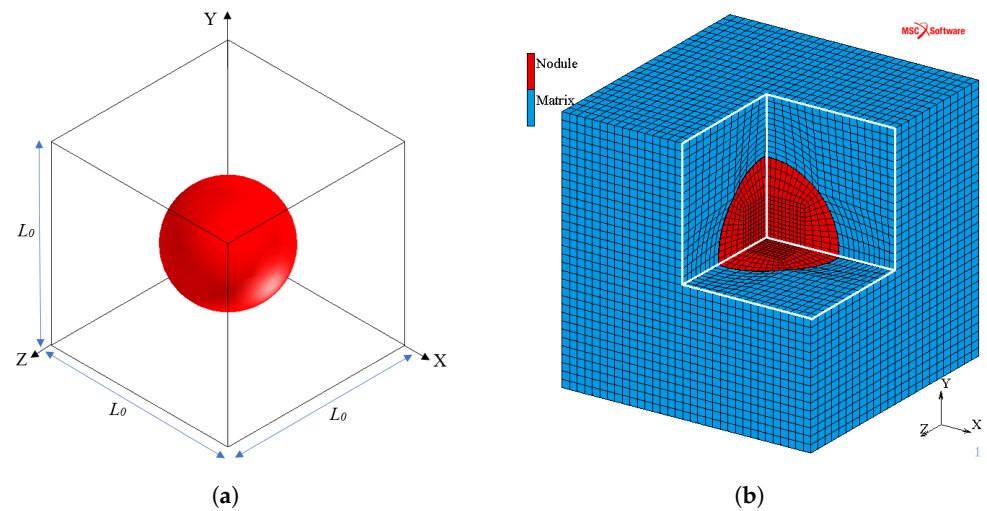


**Figure 15.** Illustration of RVE: (a) cell structure; (b) mesh.

To model the interface contact, the “node-to-segment” procedure was employed. Although, during cooling, sliding motion between matrix and nodule surfaces is unremarkable, a friction definition is needed to suppress the rigid motion of the nodule. For this purpose, the bilinear model was used [57] assuming a friction coefficient of 0.2.

Coupled thermomechanical analyses were performed and, therefore, two types of boundary conditions had to be applied. Concerning the thermal part, to simulate cooling, the temperature as a function of time was imposed uniformly on all nodes of the mesh. For the mechanical part, periodic boundary conditions [58] were applied on the cell contour using “tying” constraints [57] through the homogeneous linear constraint equation:

$$u_i^{k+} = u_i^{k-} + u_i^{RN_j} \quad (10)$$

where the superscript  $k+$  and  $k-$  represent the relative node sets on the opposite surfaces of the RVE, the subscript represents the  $i$ th direction, and  $RN_j$  indicates the specific reference node, introduced, outside the mesh, for each direction. Macroscopic stress and strain were obtained by homogenizing respective values over the cell:

$$\mathcal{E} = \langle \varepsilon \rangle = \frac{1}{V} \int_V \varepsilon dV \quad (11a)$$

$$\mathcal{\Sigma} = \langle \sigma \rangle = \frac{1}{V} \int_V \sigma dV \quad (11b)$$

where  $\mathcal{E}$  and  $\mathcal{\Sigma}$  are the logarithmic strain and the Cauchy stress tensors at the macroscale, while  $\varepsilon$  and  $\sigma$  are the strain and stress tensors in the RVE.

Large displacement, finite strain, and Lagrangian updating formulation were adopted.

Numerical analyses were performed in two steps: cooling from 769 °C at room temperature was simulated to calculate residual stresses; then, at room temperature, starting from the material state determined by cooling, a uniaxial tensile test was simulated to analyze the expected macroscopic response of the DCI.

#### 4. Simulations and Results

The proposed model was utilized to analyze the DCI studied by Zhang et al. [17]. In the paper, characterization of the microstructure of DCI after solidification is reported. Specifically, the dislocation density and elastic distortion of the crystal lattice, within the matrix, were measured around the nodules referred to as “A”, “B”, and “C” using the synchrotron 3D technique, differential aperture X-ray microdiffraction (DAXM).

The reference system for the measurements, as detailed in [59], is shown in Figure 16. Normal strain  $\epsilon_{FF}^{el}$  in the direction of the  $F$ -axis, recorded along straight paths parallel to  $Z$ -axis at different distances from it as indicated by the blue dots, was used as the measure of elastic distortion.

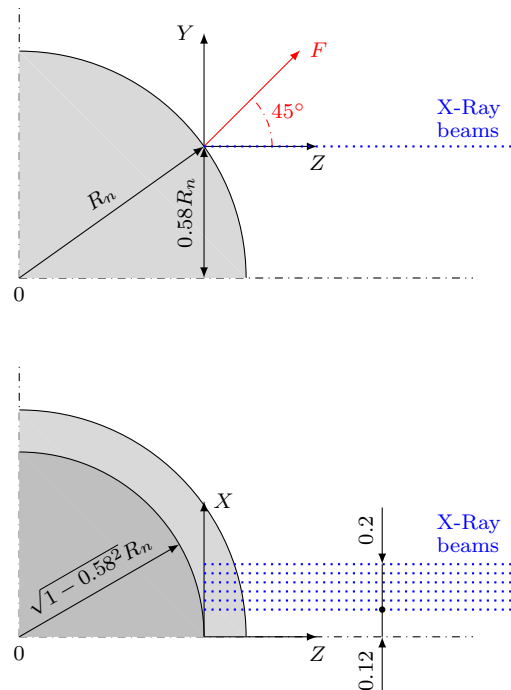


**Figure 16.** Reference system for X-ray measurements of elastic residual strain.

The dislocation density and elastic distortion of the crystal lattice are directly related to the irreversible deformation and the state of residual stresses generated during solidification, respectively. Therefore, they were used as metrics for comparison with the results of numerical simulations.

Cooling was simulated by imposing the temperature curve shown in Figure 17, which was experimentally determined in [22], as a boundary condition on all mesh nodes. It leads to the generation of a triaxial stress state, gradually becoming more severe as the temperature decreases, which varies from point to point in the cell.

Because of the different stiffnesses of the constituents, most of the stress is borne by the matrix; its components, in modulus, are highest near the contact interface and lowest at the cell boundary. In the nodule, the equivalent stress is always less than 6 MPa, which supports the choice of having assumed elastic behavior for it.

For numerical–experimental comparison, only measurements concerning nodule “A” were considered. Nodules “B” and “C” were excluded from the analysis due to their proximity, which creates a considerable divergence between the local morphology and the modeled periodic structure.

With the proposed numerical model, it is not possible to calculate the density of dislocations as measured in [17]. However, since it is related to the value of irreversible strain calculated at the end of cooling, to make a comparison, the two quantities are plotted in Figure 18 as a function of distance from the nodule normalized by its radius. Calculated strains are taken at the mesh nodes, starting at the nodule–matrix interface, approximately on the same plane (consistent with the position of the mesh nodes), and on lines parallel to those of the X-Ray beams.

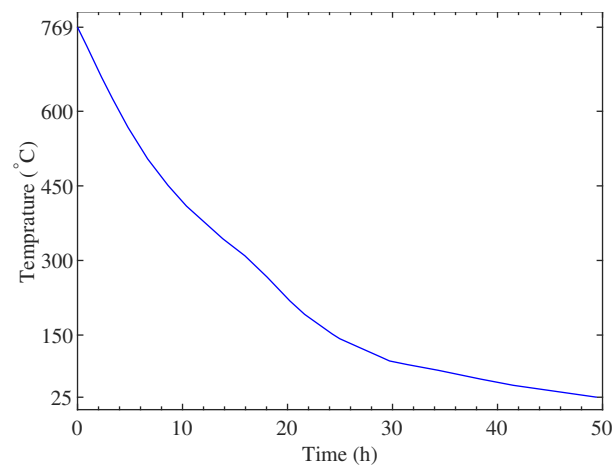


**Figure 17.** Cooling curve of the DCI, after [22].

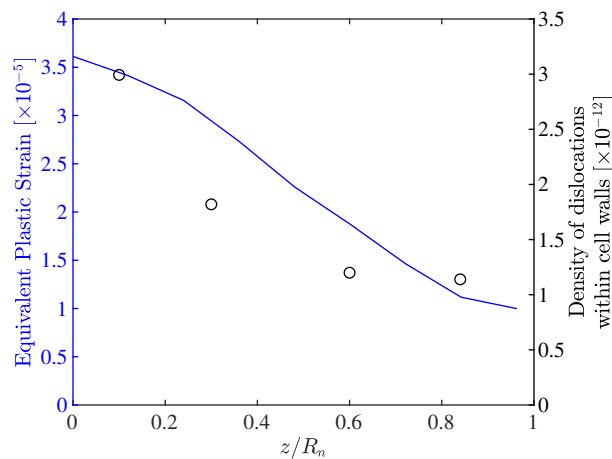


**Figure 18.** Change in dislocation density, experimental data from [17], and calculated equivalent plastic strain with the normalized distance from nodule interface.

Both quantities exhibit a maximum near the nodule and decrease monotonically as they move away from it. The qualitative finding is consistent even if the strain level is probably too low to speculate on a comparative analysis between these two quantities.

A more direct analysis can be conducted by comparing the components of elastic strain. The experimental values, digitized from [59], are plotted in Figure 19 along with the numerical predictions. The comparison shows good agreement in absolute values and trends as a function of distance from the nodule. However, experimental results show an inversion for values of  $z/R_n$  ranging from 0.3 to 0.04, depending on the position  $x/R_n$ . For the definition of the reference system and the actual size of the nodule under consideration (50  $\mu\text{m}$  in diameter), the region affected by the inversion can be identified with a shell surrounding the nodule with a thickness of about 2 to 5  $\mu\text{m}$ .

The reason for such a trend is unclear; Andriollo et al. [59] argued that the figure might be fictitious because the measurement could be affected by the sharp gradients in chemical composition. Indeed, the latter, as reported by Levine et al. [60], affects the value of the unstrained lattice spacing used as the reference to calculate the experimental strain. Finally, it is worth mentioning that, experimentally, such a trend was not observed around the “B” and “C” nodules.

An analysis was conducted to evaluate the influence of different model parts on the result. In Figure 20, the elastic deformations predicted by the full model are compared with the results obtained without considering creep. For the observed strain component, not considering creep leads to an overestimation of compression by about 15%, which leads to a deviation from the experimental evidence.

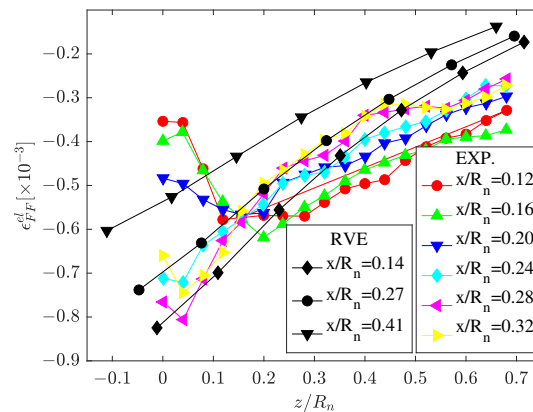


**Figure 19.** Local residual elastic strain measurement: comparison between experimental data and numerical prediction.

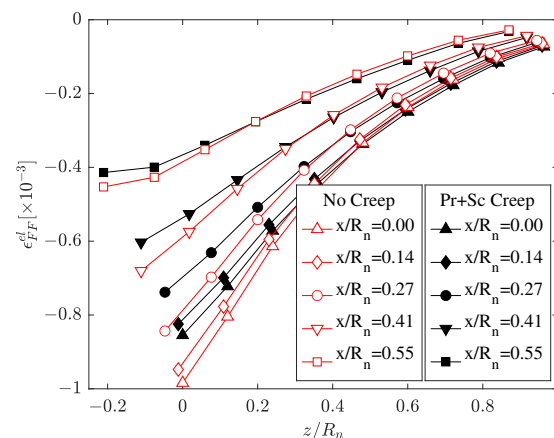


**Figure 20.** Final residual elastic strain calculated with and without considering creep.

Analyzing the two creep components separately reveals that the major contribution to relaxation is carried out by secondary creep. In Figure 21, gradual generation of  $\epsilon_{FF}^{el}$  during cooling for a point at  $z/R_n = -0.0116$  and  $x/R_n = 0.14$  is shown.

The black, blue, and red curves represent the strain component trends predicted, respectively, with the full model, considering only the secondary creep, and without considering creep.

The deviation of the black curve from the others, at about 737 °C, indicates stress relaxation due to the primary creep component. For higher temperatures, creep is inactive because the matrix's stress is less than the threshold stress. With cooling, the secondary creep (about 729 °C) is activated and quickly becomes dominant over the primary creep. Below 550 °C, creep becomes inactive as testified to by the constant offset between the three curves.

Finally, strength curves at room temperature for the uniaxial stress state were calculated (Figure 22) with different settings of the numerical model: after simulating cooling with the proposed model, blue line; after cooling with constitutive modeling that does not consider creep, green line; and without considering cooling (i.e., no residual stresses), red line.

A comparison of the curves shows that considering residual stresses has two considerable effects: first, it makes the elastic part of the curve nonlinear, resulting in a lowering of the Young's modulus to 170.9 GPa. This is consistent with what is expected for the blue curve, versus 196.8 GPa, which is an unrealistic value for DCI for the red. This difference is related to the second aspect, which is the lowering of the knee resistance of transition between elastic and plastic regimes.

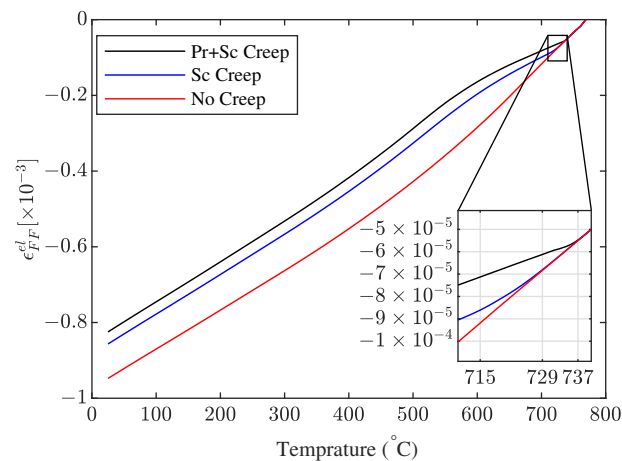


**Figure 21.** Development of residual elastic strain during cooling at  $z/R_n = -0.0116$  and  $x/R_n = 0.14$ .

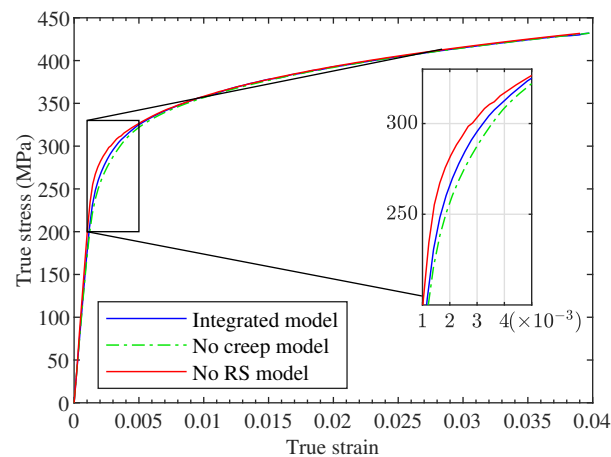


**Figure 22.** Calculated strength curves under uniaxial tension.

As the plastic deformations develop, the residual stresses gradually decrease until they cancel out, and the difference between the curves disappears at large deformations.

The contribution of creep is less obvious; it has a minimal effect on the material response that would likely be difficult to appreciate experimentally.

## 5. Conclusions

The micromechanical approach has proven to be an efficient tool for predicting the residual stress state that is generated around graphite nodules during the solidification of DCIs. Correct modeling of the mechanical behavior of the constituents is the basis of proper analysis and is critical to obtaining reliable results.

To make up for the lack of information on the physical–mechanical properties of the constituents, literature data were supplemented with those derived adopting the CALPHAD methodology. The method proved effective for the determination of thermodynamic and physical properties. However, as for mechanical properties, the approach applies only to those of broad application interest for the type of metal alloy under consideration.

Great emphasis was placed on modeling viscous behavior, which acts at high temperatures through relaxation, modeling both primary and secondary creep.

The description of the mechanical behavior of the nodule and matrix was implemented in a finite element numerical model of the RVE of cast iron. Then, it was initially used to simulate the cooling occurring in the last solidification stage and determine the state of residual stresses.

The numerical results were validated by comparison with experimental measurements using elastic distortion of the crystal lattice as a metric. Analysis of the results made

it possible to quantify the effects of the two creep contributions, showing a dominant influence of stationary creep over primary creep.

Once validated, the numerical model incorporating the residual stress state was used to simulate the uniaxial tensile test. The results show that the effect of residual stresses on the mechanical response of DCI is limited to the first part of the macroscopic stress–strain curve and vanishes at large strain.

Creep modeling, although relevant for the correct estimation of residual stresses, has a negligible effect on the mechanical response of the DCI at room temperature in terms of the uniaxial tensile strength curve.

**Author Contributions:** Conceptualization, A.R.; methodology, A.R.; software, E.K.; validation, E.K. and A.R.; investigation, E.K.; writing—original draft preparation, E.K.; writing—review and editing, A.R.; visualization, E.K.; supervision, A.R. All authors have read and agreed to the published version of the manuscript.

**Funding:** This research received no external funding.

**Data Availability Statement:** The data presented in this study are available on request from the corresponding author. The data are not publicly available as the data also forms part of an ongoing study.

**Conflicts of Interest:** The authors declare no conflict of interest.

## Appendix A

In the following, physical and mechanical properties of the matrix, calculated with JMatPro are reported:

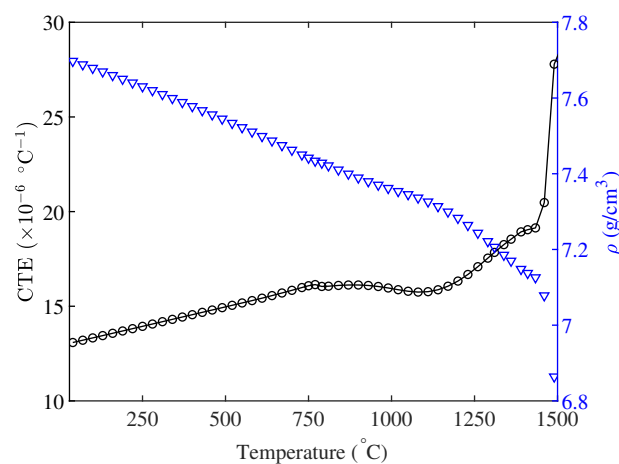


**Figure A1.** Variation of CTE and density of matrix with temperatures.

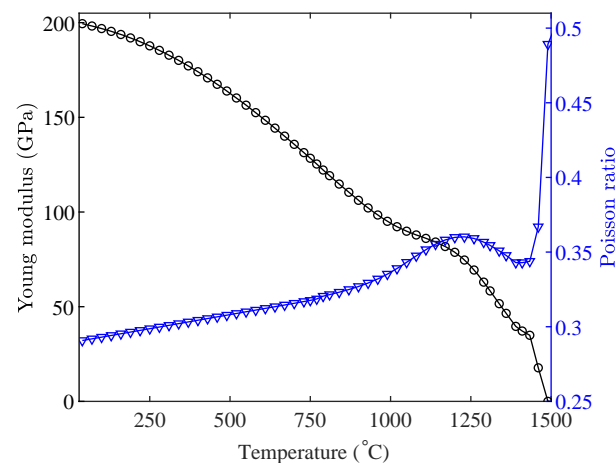


**Figure A2.** Variation of Young's modulus and Poisson's ratio of matrix with temperatures.

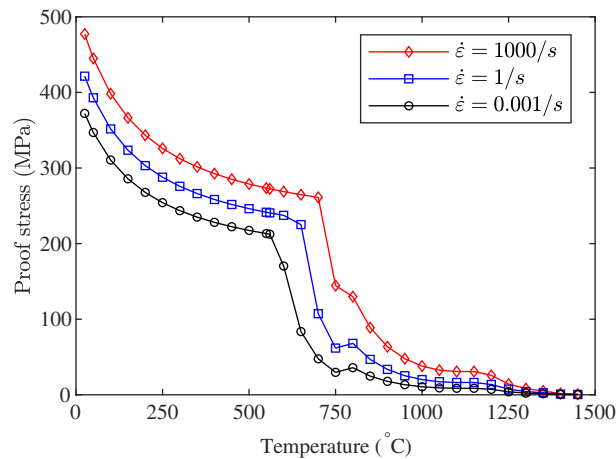


**Figure A3.** Variation of matrix proof stress with the temperature at different strain rates.

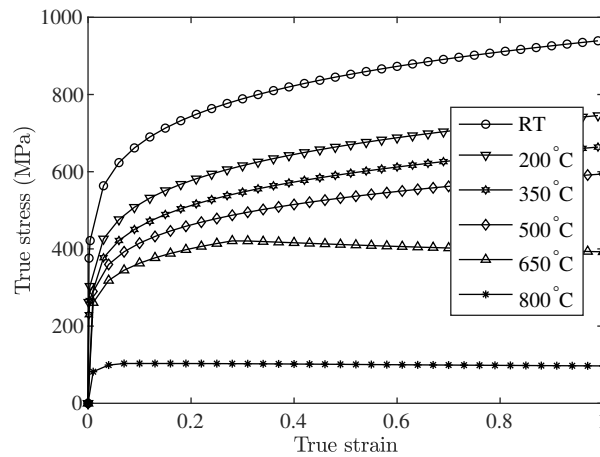


**Figure A4.** Matrix stress–strain curves at different temperatures, for  $\dot{\epsilon} = 1.0 \text{ s}^{-1}$ .

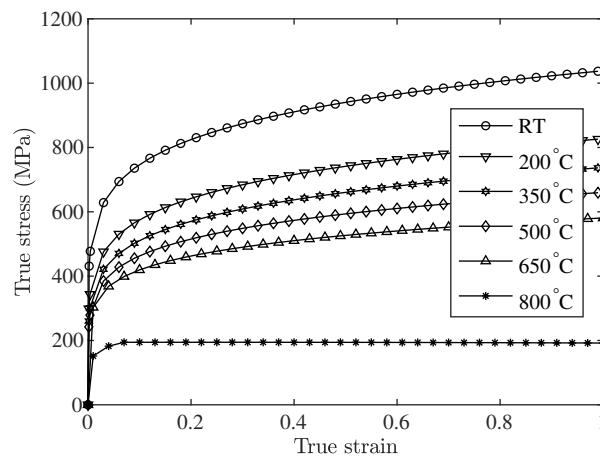


**Figure A5.** Matrix stress–strain curves at different temperatures, for  $\dot{\epsilon} = 1000 \text{ s}^{-1}$ .

## References

- Zanardi, F.; Mapelli, C.; Barella, S. Reclassification of Spheroidal Graphite Ductile Cast Irons Grades According to Design Needs. *Int. J. Met.* **2020**, *14*, 622–655. [[CrossRef](#)]
- Bai, J.; Xu, H.; Wang, Y.; Chen, X.; Zhang, X.; Cao, W.; Xu, Y. Microstructures and Mechanical Properties of Ductile Cast Iron with Different Crystallizer Inner Diameters. *Crystals* **2022**, *12*, 413. [[CrossRef](#)]
- Riposan, I.; Anca, D.; Stan, I.; Chisamera, M.; Stan, S. Graphite Nodularity Evaluation in High-Si Ductile Cast Irons. *Materials* **2022**, *15*, 7685. [[CrossRef](#)] [[PubMed](#)]

4. Stan, I.; Anca, D.; Stan, S.; Riposan, I. Solidification pattern of si-alloyed, inoculated ductile cast irons, evaluated by thermal analysis. *Metals* **2021**, *11*, 846. [[CrossRef](#)]
5. Iacoviello, F.; Di Cocco, V.; Bellini, C. Overload effects on fatigue cracks in a ferritized ductile cast iron. *Int. J. Fatigue* **2019**, *127*, 376–381. [[CrossRef](#)]
6. Iacoviello, F.; Di Cocco, V.; Bellini, C. Fatigue crack propagation and damaging micromechanisms in Ductile Cast Irons. *Int. J. Fatigue* **2019**, *124*, 48–54. [[CrossRef](#)]
7. Chaus, A.S.; Čaplovič, L.; Pokrovskii, A.I.; Sobota, R. Microstructure and Properties Evaluation of Ductile Cast Iron Subjected To Hot Plastic Deformation and Ambient Temperature Compression. *Arch. Metall. Mater.* **2023**, *68*, 639–648. [[CrossRef](#)]
8. Galkin, V.; Kurkin, A.; Gavrilov, G.; Kulikov, I.; Bazhenov, E. Investigation of the Technological Possibility of Manufacturing Volumetric Shaped Ductile Cast Iron Products in Open Dies. *Materials* **2023**, *16*, 274. [[CrossRef](#)]
9. Collini, L.; Pironi, A. Micromechanical modeling of the effect of stress triaxiality on the strain to failure of ductile cast iron. *Eng. Fract. Mech.* **2020**, *238*, 107270. [[CrossRef](#)]
10. Keough, J.R.; Hayrynen, K.L.; Pioszak, G.L. Designing with Austempered Ductile Iron (ADI). *Proc. Trans. Am. Foundry Soc.* **2010**, *118*, 503–517.
11. Zanardi, F.; Bonollo, F.; Angella, G.; Bonora, N.; Iannitti, G.; Ruggiero, A. A contribution to new material standards for ductile irons and austempered ductile irons. *Int. J. Met.* **2017**, *11*, 136–147. [[CrossRef](#)]
12. Brocks, W.; Hao, S.; Steglich, D. Micromechanical modelling of the damage and toughness behaviour of nodular cast iron materials. *J. Phys. IV JP* **1996**, *6*, C6-43–C6-52. [[CrossRef](#)]
13. Steglich, D.; Brocks, W. Micromechanical modelling of the behaviour of ductile materials including particles. *Comput. Mater. Sci.* **1997**, *9*, 7–17. [[CrossRef](#)]
14. Bonora, N.; Ruggiero, A. Micromechanical modeling of ductile cast iron incorporating damage. Part I: Ferritic ductile cast iron. *Int. J. Solids Struct.* **2005**, *42*, 1401–1424. [[CrossRef](#)]
15. Andriollo, T.; Thorborg, J.; Hattel, J. Modeling the elastic behavior of ductile cast iron including anisotropy in the graphite nodules. *Int. J. Solids Struct.* **2016**, *100–101*, 523–535. [[CrossRef](#)]
16. Pereira, A.; Costa, M.; Anflor, C.; Pardal, J.; Leiderman, R. Estimating the effective elastic parameters of nodular cast iron from micro-tomographic imaging and multiscale finite elements: Comparison between numerical and experimental results. *Metals* **2018**, *8*, 695. [[CrossRef](#)]
17. Zhang, Y.B.; Andriollo, T.; Fæster, S.; Liu, W.; Hattel, J.; Barabash, R.I. Three-dimensional local residual stress and orientation gradients near graphite nodules in ductile cast iron. *Acta Mater.* **2016**, *121*, 173–180. [[CrossRef](#)]
18. Zhang, Y.B.; Andriollo, T.; Fæster, S.; Barabash, R.; Xu, R.; Tiedje, N.; Thorborg, J.; Hattel, J.; Juul Jensen, D.; Hansen, N. Microstructure and residual elastic strain at graphite nodules in ductile cast iron analyzed by synchrotron X-ray microdiffraction. *Acta Mater.* **2019**, *167*, 221–230. [[CrossRef](#)]
19. Krasowsky, A.J.; Kramarenko, I.V.; Kalaida, V.V. Fracture toughness of nodular graphite cast irons under static, impact and cyclic loading. *Fatigue Fract. Eng. Mater. Struct.* **1987**, *10*, 223–237. [[CrossRef](#)]
20. Iannitti, G.; Ruggiero, A.; Bonora, N.; Masaggia, S.; Veneri, F. Micromechanical modelling of constitutive behavior of austempered ductile iron (ADI) at high strain rate. *Theor. Appl. Fract. Mech.* **2017**, *92*, 351–359. [[CrossRef](#)]
21. Andriollo, T.; Zhang, Y.; Fæster, S.; Thorborg, J.; Hattel, J. Impact of micro-scale residual stress on in-situ tensile testing of ductile cast iron: Digital volume correlation vs. model with fully resolved microstructure vs. periodic unit cell. *J. Mech. Phys. Solids* **2019**, *125*, 714–735. [[CrossRef](#)]
22. Andriollo, T.; Hellström, K.; Sonne, M.R.; Thorborg, J.; Tiedje, N.; Hattel, J. Uncovering the local inelastic interactions during manufacture of ductile cast iron: How the substructure of the graphite particles can induce residual stress concentrations in the matrix. *J. Mech. Phys. Solids* **2018**, *111*, 333–357. [[CrossRef](#)]
23. Kaufman, L.; Bernstein, H. *Computer Calculation of Phase Diagrams: With Special Reference to Refractory Metals*; Academic Press Inc.: New York, NY, USA, 1970; Volume 4, p. 344.
24. Saunders, N.; Guo, Z.; Li, X.; Miodownik, A.P.; Schillé, J.P. Using JMatPro to model materials properties and behavior. *Jom* **2003**, *55*, 60–65. [[CrossRef](#)]
25. Ductile Iron Society. *Ductile Iron Data for Design Engineers*; Ductile Iron Society: Germantown, WI, USA, 1990.
26. American Foundrymen’s Society. *Ductile Iron Handbook*; American Foundrymen’s Society: Des Plaines, IL, USA, 1993; p. 277.
27. Andriollo, T.; Thorborg, J.; Tiedje, N.; Hattel, J. A micro-mechanical analysis of thermo-elastic properties and local residual stresses in ductile iron based on a new anisotropic model for the graphite nodules. *Model. Simul. Mater. Sci. Eng.* **2016**, *24*, 55012. [[CrossRef](#)]
28. Kohout, J. A simple relation for deviation of grey and nodular cast irons from Hooke’s law. *Mater. Sci. Eng. A* **2001**, *313*, 16–23. [[CrossRef](#)]
29. Angus, H.T. *Cast Iron: Physical and Engineering Properties*; Elsevier: Amsterdam, The Netherlands, 1976. [[CrossRef](#)]
30. Speich, G.R.; Schwoeble, A.J.; Kapadia, B.M. Elastic moduli of gray and nodular cast iron. *J. Appl. Mech. Trans. ASME* **1980**, *47*, 821–826. [[CrossRef](#)]
31. Hervas, I. Contribution à l’Étude des Mécanismes d’Endommagement des Fontes Ferritiques à Graphite Sphéroïdal: Influence de la Température, du Trajet de Chargement et rôle des Interfaces Nodules/Matrice. Ph.D. Thesis, University of Caen Normandy, Caen, France, 2013.

32. Kuna, M.; Sun, D.Z. Three-dimensional cell model analyses of void growth in ductile materials. *Int. J. Fract.* **1996**, *81*, 235–258. [[CrossRef](#)]
33. Sherby, O.D.; Burke, P.M. Mechanical behavior of crystalline solids at elevated temperature. *Prog. Mater. Sci.* **1968**, *13*, 323–390. [[CrossRef](#)]
34. Esposito, L.; Bonora, N. A primary creep model for Class M materials. *Mater. Sci. Eng. A* **2011**, *528*, 5496–5501. [[CrossRef](#)]
35. Mukherjee, A.K.; Bird, J.E.; Dorn, J.E. *Experimental Correlations for High-Temperature Creep*; Technical Report; University of California, Lawrence Berkeley National Laboratory: Berkeley, CA, USA, 1968.
36. Bird, J.; Mukherjee, A.; Dorn, J.E. *Correlations between High-Temperature Creep Behavior and Structure*; Technical Report; University of California, Lawrence Berkeley National Laboratory: Berkeley, CA, USA, 1969.
37. Lagneborg, R.; Bergman, B. The stress/creep rate behaviour of precipitation-hardened alloys. *Met. Sci.* **1976**, *10*, 20–28. [[CrossRef](#)]
38. Evans, W.J.; Harrison, G.F. The development of a universal equation for secondary creep rates in pure metals and engineering alloys. *Met. Sci.* **1976**, *10*, 307–313. [[CrossRef](#)]
39. Davies, P.W.; Nelmes, G.; Williams, K.R.; Wilshire, B. Stress-change experiments during high-temperature creep of copper, iron, and zinc. *Met. Sci. J.* **1973**, *7*, 87–92. [[CrossRef](#)]
40. Parker, J.D.; Wilshire, B. The Effect of a Dispersion of Cobalt Particles on High-Temperature Creep of Copper. *Met. Sci.* **1975**, *9*, 248–252. [[CrossRef](#)]
41. Lund, R.W.; Nix, W.D. High temperature creep of Ni-20Cr-2ThO<sub>2</sub> single crystals. *Acta Metall.* **1976**, *24*, 469–481. [[CrossRef](#)]
42. Kaibyshev, R.; Kazakulov, I. Deformation behavior of Fe - 3Si steel. *Mater. Sci. Technol.* **2004**, *20*, 221–228. [[CrossRef](#)]
43. Barrett, C.R. The Influence of Grain Boundaries and Stacking Faults on High Temperature Plastic Deformation. Ph.D. Thesis, Stanford University, Stanford, CA, USA, 1964.
44. Stang, R.G.; Nix, W.D.; Barrett, C.R. High temperature creep in Fe-3 pct Si. *Metall. Trans.* **1973**, *4*, 1695–1699. [[CrossRef](#)]
45. Stang, R.G.; Nix, W.D.; Barrett, C.R. The influence of subgrain boundaries on the rate controlling creep processes in Fe-3 Pct Si. *Metall. Trans. A* **1975**, *6*, 2065–2071. [[CrossRef](#)]
46. Mohamed, F.A.; Park, K.T.; Lavernia, E.J. Creep behavior of discontinuous SiC-Al composites. *Mater. Sci. Eng. A* **1992**, *150*, 21–35. [[CrossRef](#)]
47. Madelung, O. (Ed.) *Diffusion in Solid Metals and Alloys*; Springer: Berlin/Heidelberg, Germany, 1990; Volume 26. [[CrossRef](#)]
48. Cottrell, A. *An Introduction to Metallurgy*; The Institute of Materials: London, UK, 1995; p. 548.
49. Frost, H.J.; Ashby, M.F. *Deformation-Mechanism Maps: The Plasticity and Creep of Metals and Ceramics*, 1st ed.; Pergamon Press: Oxford, UK; New York, NY, USA, 1982; p. 166.
50. Cadek, J. *Creep in Metallic Materials*; Elsevier Science Publishers B.V.: Amsterdam, The Netherlands, 1988; Volume 48.
51. Hervas, I.; Bettaieb, M.B.; Thuault, A.; Hug, E. Graphite nodule morphology as an indicator of the local complex strain state in ductile cast iron. *Mater. Des.* **2013**, *52*, 524–532. [[CrossRef](#)]
52. Colonna, F.; Los, J.H.; Fasolino, A.; Meijer, E.J. Properties of graphite at melting from multilayer thermodynamic integration. *Phys. Rev. B-Condens. Matter Mater. Phys.* **2009**, *80*, 1–8. [[CrossRef](#)]
53. Delprete, C.; Sesana, R. Experimental characterization of a Si-Mo-Cr ductile cast iron. *Mater. Des.* **2014**, *57*, 528–537. [[CrossRef](#)]
54. Tsang, D.K.; Marsden, B.J.; Fok, S.L.; Hall, G. Graphite thermal expansion relationship for different temperature ranges. *Carbon* **2005**, *43*, 2902–2906. [[CrossRef](#)]
55. Riley, D. The thermal expansion of graphite: Part II. Theoretical. *Proc. Phys. Soc.* **1945**, *57*, 486. [[CrossRef](#)]
56. Monchoux, J.P.; Verdu, C.; Thollet, G.; Fougères, R.; Reynaud, A. Morphological changes of graphite spheroids during heat treatment of ductile cast irons. *Acta Mater.* **2001**, *49*, 4355–4362. [[CrossRef](#)]
57. MSC Software Corporation. *MSC Marc Volume A: Theory and User Information*; MSC Software Corporation: Newport Beach, CA, USA, 2019.
58. Hill, R. Elastic properties of reinforced solids: Some theoretical principles. *J. Mech. Phys. Solids* **1963**, *11*, 357–372. [[CrossRef](#)]
59. Andriollo, T.; Fæster, S.; Winther, G. Probing the structure and mechanical properties of the graphite nodules in ductile cast irons via nano-indentation. *Mech. Mater.* **2018**, *122*, 85–95. [[CrossRef](#)]
60. Levine, L.E.; Okoro, C.; Xu, R. Full elastic strain and stress tensor measurements from individual dislocation cells in copper through-Si vias. *IUCrJ* **2015**, *2*, 635–642. [[CrossRef](#)]

**Disclaimer/Publisher’s Note:** The statements, opinions and data contained in all publications are solely those of the individual author(s) and contributor(s) and not of MDPI and/or the editor(s). MDPI and/or the editor(s) disclaim responsibility for any injury to people or property resulting from any ideas, methods, instructions or products referred to in the content.